

Self-assembly of carboxylated polythiophene nanowires for improved bulk heterojunction morphology in polymer solar cells†

Weiwei Li,^{‡,ab} Brian J. Worfolk,^{‡,ab} Peng Li,^b Tate C. Hauger,^{ab} Kenneth D. Harris^b and Jillian M. Buriak^{*ab}

Received 30th January 2012, Accepted 15th April 2012

DOI: 10.1039/c2jm30576c

Conjugated regioregular poly[3-(5-carboxypentyl) thiophene-2,5-diyl] (P3CPenT), a derivative of poly(3-hexylthiophene) (P3HT), is introduced as a hole transport layer (HTL) for P3HT:PCBM plastic solar cells (PSCs). P3CPenT, a carboxyl-functionalized polythiophene, is insoluble in solvents typically used in the preparation of photoactive layers such as chloroform, chlorobenzene and dichlorobenzene, allowing successive processing of the photoactive layer without dissolution of the HTL. P3CPenT self-assembles into nanowires in DMSO solution and when cast as a film, reduces concentration gradients of P3HT:PCBM photoactive layers. P3HT:PCBM PSCs incorporating P3CPenT nanowires as the HTL have a higher fill factor (FF, 0.67) and power conversion efficiency (PCE, 3.7%) than devices with conventional PEDOT:PSS HTLs.

1. Introduction

Polymer solar cells (PSCs) based on bulk-heterojunction (BHJ) structures with conjugated materials as electron donors and fullerene derivatives as electron acceptors have made great progress in the past decades.^{1–3} Device performance, longevity, and cost are all determining factors for widespread adoption of the technology, and by optimizing the PSC device structure and fabrication route, considerable progress has been made in each of these areas.^{1,3–5} In particular, high power conversion efficiencies (PCEs) above 7% have been achieved for new low band gap conjugated materials,^{6–12} indicating a bright future for PSCs. Typically, PSCs consist of transparent indium tin oxide (ITO) as the anode for hole collection, a metal cathode for electron collection, a BHJ photoactive layer for light absorption and charge generation, and interfacial layers between each electrode and the active layer to facilitate charge extraction. One of these interfacial layers, the hole transport layer (HTL), is applied between the anode and photoactive layer to reduce the hole extraction barrier, block electrons, and improve the interface roughness.^{13–16}

Poly(3,4-ethylenedioxythiophene):poly(styrenesulfonate) (PEDOT:PSS) has been intensively studied and has several advantages as an HTL.^{15,17} It adjusts the work function of ITO to a value near the highest occupied molecular orbital (HOMO) of

common donor materials;¹⁸ it is insoluble in most organic solvents allowing for solution processing of subsequent layers; it is transparent in the visible range;¹⁹ and it has high electrical conductivity compared to other organic HTLs.²⁰ Disadvantages, however, have also been identified: the acidity of PEDOT:PSS (pH \approx 1) can decrease PSC lifetime through etching of ITO;^{21,22} PEDOT:PSS is hygroscopic and tends to absorb water, increasing device resistance and reducing efficiency;^{22,23} and Na⁺PSS[−] tends to migrate and react with components of the active layer and Al electrode.^{24,25} Moreover, while PEDOT:PSS can modify the work function of ITO,²⁶ it can still form non-ohmic contacts with low band gap polymers having higher HOMO levels,²⁷ and X-ray photoelectron spectroscopy (XPS) analysis has revealed that some BHJ combinations, including poly(3-hexylthiophene):[6,6]-phenyl-C₆₁-butyric acid methyl ester (P3HT:PCBM), suffer from detrimental concentration gradients when cast on PEDOT:PSS.^{28,29} In this situation, additional annealing steps are required to improve morphology.³⁰ Substitutes for PEDOT:PSS include inorganic oxide materials such as NiO,^{31–34} WO₃,³⁵ MoO_x,³⁶ IrO_x,³⁷ V₂O₅,³⁸ Cu₂O nanocrystals,³⁹ Au nanoparticles,⁴⁰ organic materials,^{41,42} graphene oxide,⁴³ polythiophene,⁴⁴ and high molecular weight P3HT.⁴⁵

In this work, we introduce the carboxylated P3HT derivative poly[3-(5-carboxypentyl)thiophene-2,5-diyl] (P3CPenT) as an HTL to directly replace PEDOT:PSS (Fig. 1a). This carboxylated P3HT derivative has been successfully used in dye-sensitized^{46–48} and hybrid solar cells,^{49–51} and in our own previous work, carboxylated polythiophenes were used with C₆₀ nanocolumns deposited *via* glancing angle deposition (GLAD)⁵² or as a BHJ with PCBM resulting in a PCE of 2.6%.⁵³ Here, we observe the self-assembly of P3CPenT into 10–20 nm diameter nanowires (NWs) after simply dispersing the polymer in dimethyl sulfoxide (DMSO). Jenekhe *et al.* have shown improved charge

^aDepartment of Chemistry, University of Alberta, Edmonton, Alberta, T6G 2G2, Canada. E-mail: jburiaak@ualberta.ca

^bNational Institute for Nanotechnology, 11421 Saskatchewan Drive, Edmonton, Alberta, T6G 2M9, Canada

† Electronic supplementary information (ESI) available: Surface energy calculations, cross sectional TEM analysis and stability testing. See DOI: 10.1039/c2jm30576c

‡ These two authors have equally contributed to this study.

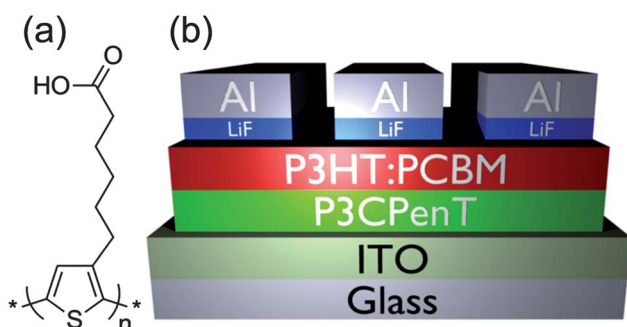


Fig. 1 (a) Chemical structure of poly[3-(5-carboxypentyl)thiophene-2,5-diyl] (P3CPenT) used to self-assemble nanowires for use as the hole transport layer in plastic solar cells. (b) The device architecture of plastic solar cells consisting of: ITO/P3CPenT/P3HT:PCBM/LiF/Al.

transport and significant enhancements in photovoltaic performance when self-assembled polythiophene-based NWs were used in the photoactive layer as a result of increased hole mobility and charge transport.^{54,55} In our case, we apply P3CPenT NWs from DMSO solution as an HTL beneath a P3HT:PCBM photoactive layer: the pendant carboxyalkyl group renders the P3CPenT NWs insoluble in common photoactive layer solvents such as chloroform, chlorobenzene (CB) and dichlorobenzene (DCB), allowing conventional BHJ active layers to be applied over P3CPenT films using standard spin casting procedures. Due to their similar conjugated backbones, the P3CPenT derivative has energy levels similar to the donor, and thus charge transfer across the P3CPenT/P3HT interface is energetically favourable. Transmission electron microscopy (TEM) is used to characterize the impact of different HTLs (no HTL, PEDOT:PSS or P3CPenT NWs) on the morphology of the BHJ and the associated influence on photovoltaic device performance.

2. Experimental

2.1 Materials and film preparation

All chemicals were purchased from commercial suppliers and used without further purification. P3CPenT and P3HT were purchased from Rieke Metals, Inc. PCBM, PEDOT:PSS and Al (99.99%) were purchased from American Dye Source (ADS61BFA), Heraeus (Clevios P VP Al 4083) and Kurt J. Lesker respectively. ITO coated glass substrates ($8\text{--}12\ \Omega\ \square^{-1}$) were purchased from Delta Technologies Ltd., and all solvents and LiF were purchased from Sigma Aldrich.

The self-assembly of P3CPenT NWs was performed by dissolving P3CPenT ($1\ \text{mg mL}^{-1}$ to $15\ \text{mg mL}^{-1}$) in DMSO and stirring for 12 h at $90\ ^\circ\text{C}$ in an inert environment, followed by cooling to room temperature. Films were fabricated by directly spin coating the NW solution on freshly cleaned ITO at different rotation speeds in air to achieve different thicknesses. All samples were subsequently annealed in air for 10 min at $90\ ^\circ\text{C}$. To form P3CPenT films by adsorption from solution, ITO was first cleaned then immersed in a $4\ \text{mg mL}^{-1}$ P3CPenT solution in DMSO for 24 h. The modified substrates were then thoroughly rinsed with DMSO, ultrasonicated in DMSO for 30 min, spin

dried at 3000 rpm and finally heated to $90\ ^\circ\text{C}$ for 10 min. The thickness of P3CPenT film was determined by AFM, as shown in Fig. S1†.

2.2 Device fabrication

PSCs were fabricated with the device configuration ITO/HTL/P3HT:PCBM/LiF/Al, in which the HTL was either PEDOT:PSS or P3CPenT. ITO-coated glass substrates were cleaned by successive 10 min ultrasonications in methylene chloride, Millipore water ($18\ \text{M}\Omega\ \text{cm}$) and 2-propanol followed by a 10 min air plasma treatment at ~ 0.1 Torr (Harrick Plasma, PDC 32G, 18 W). Self-assembled P3CPenT NW films were formed as described above. Specifically, P3CPenT NW films with 8 nm thickness were prepared by spin-coating $5\ \text{mg mL}^{-1}$ P3CPenT solution in DMSO at 3000 rpm for 3 min. For reference cells in which PEDOT:PSS acted as the HTL, aqueous PEDOT:PSS solution was passed through a $0.2\ \mu\text{m}$ cellulose acetate filter directly onto the cleaned ITO substrates and spin-cast at 3500 rpm for 1 min to form a layer ~ 30 nm thick. To form PEDOT:PSS films of different thicknesses, the spin coating speed and solution concentration were varied. All PEDOT:PSS samples were annealed in air for 10 min at $125\ ^\circ\text{C}$.

For all PSC photoactive layers, individual $23\ \text{mg mL}^{-1}$ solutions of P3HT and PCBM in DCB were prepared in an inert argon atmosphere and stirred at $\sim 60\ ^\circ\text{C}$ for several hours. Following stirring, the individual solutions were combined 1 : 1 by weight, stirred, and spin-cast at 600 rpm for 1 min in air. The samples were then covered and dried over the course of 15–20 min. The thickness of the P3HT:PCBM active layer was 200 ± 10 nm. Devices were completed by thermal evaporation of $0.6\ \text{nm}$ of LiF and $80\ \text{nm}$ of aluminium, forming a device area of $0.20\ \text{cm}^2$.

2.3 Characterization of PSCs

Photovoltaic performance was measured in air under AM 1.5 G simulated solar irradiation with a xenon solar simulator (Oriel 91191 1000W). The testing irradiance was calibrated against a certified Si reference cell fitted with a KG-5 filter (model PVM624, PV Measurements, Inc.). Device $J\text{--}V$ characteristics were measured using a Keithley 2400 source meter. Devices for stability testing were stored inside a glove box under a nitrogen atmosphere between testing periods and were tested at ambient conditions in air.

2.4 Characterization of P3CPenT films

The energy levels of P3CPenT, P3HT and PCBM were investigated using cyclic voltammetry (Princeton Applied Research Potentiostat model 2273) with a standard three-electrode electrochemical cell. A glassy carbon working electrode, a Pt wire counter electrode, and a Ag/AgNO₃ reference electrode were used, and the electrolyte was $0.1\ \text{M}$ tetrabutylammonium hexafluorophosphate (*n*Bu₄NPF₆) in acetonitrile solution. The reference potential was calibrated to a ferrocene redox couple, and a scan rate of $100\ \text{mV s}^{-1}$ was employed. X-ray photoelectron spectroscopy (XPS, Kratos Analytical, Axis-Ultra) was performed using monochromatic Al K_α X-ray irradiation at a photon energy of $1486.6\ \text{eV}$ on P3CPenT films

cast by both spin coating and absorption from solution. The XPS instrument was calibrated using the C(1s) signal (BE = 284.9 eV).

Work functions of the modified ITO surfaces were determined by ultraviolet photoelectron spectroscopy (UPS) using the He I line ($h\nu = 21.2$ eV). The power for UPS was $3 \text{ kV} \times 10 \text{ mA}$ (30 W), and samples were biased at -10 V during all measurements to observe the secondary electron edge. The average and standard deviation of three spots on the same sample are reported. Contact angle measurements were conducted using a Rame-Hart NRL C.A. contact angle goniometer system (No. 100-00) using water and *n*-hexadecane under ambient conditions ($22 \text{ }^\circ\text{C}$). A Nanoscope IV (Digital Instruments/Veeco) instrument, operated in tapping mode with commercially available Si cantilevers (Asylum Research, 300 kHz), was used for atomic force microscopy. To determine the thickness of organic films, the same instrument was operated in contact mode to excavate a section of the organic material, and then the trench depth was measured in tapping mode.

For transmission electron microscopy, P3CPenT solution in DMSO (0.1 mg mL^{-1}) was dropped onto carbon-coated TEM grids and imaged with a JEOL JEM 2100 TEM at a 120 kV acceleration voltage. For cross sectional TEM imaging, Si substrates were first cleaned and treated with air plasma, the HTL layers were applied as described above, and P3HT:PCBM active layers were then spin-cast on top of the HTL layer. Cross sectional TEM samples were prepared using a Hitachi NB 5000 FIB/SEM dual beam system. Two protection layers (30 nm sputtered carbon, and $1 \mu\text{m}$ FIB-assisted sputtered tungsten) were deposited first to avoid Ga ion beam damage to the films during subsequent FIB processing. TEM lamellae sections were rough milled and transferred onto a TEM grid using a 40 kV primary Ga^+ beam and subsequently thinned/polished using a 10 kV primary Ga^+ beam to a thickness of less than 100 nm. Bright-field TEM images were acquired on a JEOL 2200FS TEM/STEM at 200 kV accelerating voltage.

X-ray diffraction (XRD) was performed using a Bruker D8 Discover instrument with a Cu- K_α beam (40 kV, 40 mA; $\lambda = 1.541784 \text{ \AA}$) and operated at a glancing angle, $\omega = 2^\circ$. For these XRD measurements, P3CPenT NW samples were spin-casted from DMSO solution on clean Si wafers, and peaks in the XRD pattern were identified in terms of the Bragg angle, 2θ , and calibrated to a LaB_6 NIST standard (SRM-660b). The integration time for all samples was 1 h. Optical absorption or transmission spectra were measured on an Agilent 8453 UV-Vis Spectrophotometer.

3. Results and discussion

3.1 Self-assembly of P3CPenT nanowires

The self-assembly of polythiophene-based NWs through the interdigitation of alkyl chains and lamellar packing in homopolymers and block copolymers has been extensively studied by Jenekhe *et al.*^{54–59} Typically poor solvents or storage in dark, vibrationless environments for $\sim 72 \text{ h}$ are required for self-assembly to occur.^{60–63} Using a similar motif, we added P3CPenT to DMSO at $90 \text{ }^\circ\text{C}$, resulting in an orange solution. This was stirred for 12 h, and subsequently cooled to room

temperature, yielding a purple coloured solution within $\sim 30 \text{ s}$. Optical absorbance of P3CPenT solutions in pyridine and DMSO (after heating and cooling to room temperature, as described in the Experimental) are shown in Fig. 2a, and the observed wavelengths of peak absorbance (λ_{max}) were 449 nm and 480 nm in pyridine and DMSO, respectively. The bathochromic shift observed in DMSO is indicative of increased effective conjugation length, often the result of increased molecular ordering (higher degree of coplanar alignment in the thiophene backbone).⁵⁸ Additional prominent features in the DMSO solution absorbance spectrum are two shoulders at 547 nm and 594 nm. Typically these peaks are characteristic of additional electronic transitions based on π -stacking of polymer chains, as the result of increased molecular ordering.^{58,60,64} The absence of these shoulders for P3CPenT in pyridine indicates dissolution, and a lack of self-assembled molecular ordering, in contrast to the semicrystalline self-assembled morphology in DMSO (as evidenced through increased coplanar ordering of the thiophene backbone and π -stacking of polymer chains, *vide supra*). UV-vis absorbance spectra for solid-state P3CPenT thin films cast from DMSO and pyridine

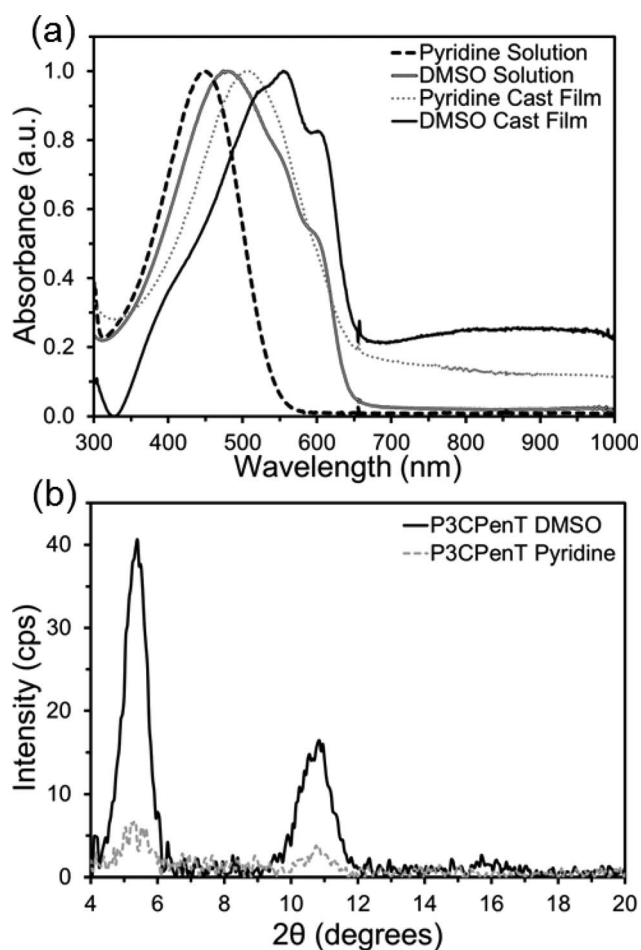


Fig. 2 (a) Solution UV-vis spectra of P3CPenT in pyridine and DMSO solutions and solid-state UV-vis spectra of P3CPenT thin films cast from pyridine and DMSO solutions. (b) XRD spectra from P3CPenT films cast from DMSO and pyridine on Si substrates.

solutions are also included in Fig. 2a, and in both cases, solid-state spectra are red-shifted compared to the corresponding solution spectra. Spectra for the films cast from DMSO are also red-shifted compared to pyridine-cast counterparts, with the λ_{\max} shifting from 505 nm to 552 nm, and peaks characteristic of π -stacking are evident only in the DMSO-cast films at 552 nm and 599 nm. These results indicate increased π -stacking in DMSO-cast films.⁵⁸ Both DMSO- and pyridine-cast films also appear to have non-zero absorption above 650 nm, possibly indicative of doping and the associated generation of charge carriers.

As shown in Fig. 1a, P3CPenT bears carboxyl groups on pentyl side chains attached to the polythiophene backbone. In our previous work, hydrogen bonds originating from the carboxyl groups were identified by Fourier transform infrared spectroscopy (FTIR) measurements of pyridine : chlorobenzene (1 : 6, v/v) cast films.⁵³ In the present work, the crystalline structures of P3CPenT films spin cast from DMSO and pyridine solutions were studied by XRD. The spectrum in Fig. 2b for the film cast from DMSO shows peaks at $2\theta = 5.4^\circ$ and 10.8° , which are attributed to carboxyalkyl chain stacking along the (100) and (200) directions, respectively. The measured (100) d-spacing was 16.4 Å, which is similar to the (100) d-spacing of 16.8 Å previously reported for pyridine : chlorobenzene (1 : 6, v/v) cast films of P3CPenT.⁵³ The XRD peaks indicate crystalline lamellar packing of P3CPenT units, and applying the Scherrer equation to the (100) peak allows us to determine an average spherical crystallite size of 11.9 nm.⁶⁵ Similar P3CPenT films cast from pyridine had XRD peaks in the same positions, but these peaks were much weaker and showed significantly reduced crystal sizes (5.7 nm) compared to DMSO-cast films (Fig. 2b). This observation is consistent with the UV-vis absorbance data and supports the claim that DMSO-cast P3CPenT films are more crystalline than pyridine-cast counterparts. McCullough *et al.* reported on the self-assembly of poly[3-(2-carboxyethyl)thiophene-2,5-diyl] (P3CET), which has an ethyl linker instead of the pentyl chain in P3CPenT.⁶⁶ P3CET was shown to self-assemble *via* hydrophobic interactions that were stabilized by hydrogen bonding, as characterized by the presence of a carboxylic acid dimer stretch in the infrared spectrum.⁶⁶ As such, we hypothesize that hydrogen bonding formation of dimers, aids in the molecular structuring of P3CPenT NW films.

The morphology of P3CPenT NW films cast from a low concentration (0.1 mg mL⁻¹) DMSO solution was characterized by transmission electron microscopy (TEM) and atomic force microscopy (AFM) as shown in Fig. 3. TEM analysis reveals the presence of P3CPenT NWs with an average width of 8.0 ± 1.0 nm. It is difficult to characterize the length of the NWs because they form an interconnected network, and endpoints cannot be identified. As seen by AFM in Fig. 3b, the average width is 9–10 nm, which is slightly larger than the TEM measurements and is likely the result of tip convolution effects.⁶⁷ As can be seen from AFM, the P3CPenT NWs appear to be made up of smaller interconnected segments that are about 70 ± 30 nm in length, calculated from an average of 50 measurements. Both TEM and AFM, when coupled with the XRD and UV-Vis results, confirm the presence of semi-crystalline P3CPenT NWs.

3.2 Surface properties of ITO modified by P3CPenT

To characterize the chemical and electronic properties of the interfaces, films of P3CPenT were analysed by X-ray photoelectron spectroscopy (XPS) and compared to untreated ITO substrates. The spectra are shown in Fig. 4. The XPS spectra of the S(2p) region show distinctive sulfur peaks only in samples modified with P3CPenT. This signal originates in the polythiophene backbone and indicates the presence of the P3CPenT layer. For unmodified ITO surfaces, the binding energy peak for Sn(3d) is present at 495.0 eV, and binding energy peaks for In(3d) are found at 444.6 eV and 452.2 eV. When modified with P3CPenT, the binding energy peaks shift to higher energies of 497.4 eV for Sn(3d), and 445.8 eV and 453.4 eV for In(3d), indicating surface modification.⁶⁸

Fig. 5a illustrates the energy levels of the electronic materials in this work. The values for P3CPenT, P3HT and PCBM were measured by electrochemical cyclic voltammetry,⁵³ and the work functions of ITO and Al are from literature.⁶⁹ The HOMO energy of P3CPenT is -5.1 eV, which as predicted, is the same as the HOMO level of P3HT. The similarity between these two values should lower the energy barrier for charge transfer and allow efficient hole transport between P3HT and P3CPenT. Ultraviolet photoelectron spectroscopy (UPS) was utilized to determine the surface work functions of unmodified ITO, P3CPenT-modified ITO, and PEDOT:PSS-modified ITO. As shown in Fig. 5b, when ITO was modified by PEDOT:PSS or P3CPenT, the secondary electron cutoff slightly shifts to greater kinetic energies, indicating an increased surface work function. The measured values are 4.78 ± 0.01 eV, 4.80 ± 0.01 eV and 4.86 ± 0.03 eV for unmodified ITO, PEDOT:PSS-modified ITO and P3CPenT-modified ITO, respectively. Moreover, we found that the work function did not vary strongly with P3CPenT thickness in our measurements of 8, 12, and 36 nm films (see Fig. S2†).

3.3 Investigation of vertical concentration gradients by cross section TEM

Contact angles of ITO, PEDOT:PSS-modified ITO, and P3CPenT-modified ITO with water and *n*-hexadecane were determined on freshly cleaned surfaces, and the results are summarized in Table 1. Low contact angles were observed for unmodified ITO both with water and with *n*-hexadecane (9° and 9°),⁶⁸ and roughly similar values were recorded for ITO modified by PEDOT:PSS (4° in water and 10° in *n*-hexadecane). The contact angles for P3CPenT-modified ITO were significantly different: 47° in water and 3° in *n*-hexadecane, indicating a more hydrophobic surface despite the prevalence of hydrophilic hydrogen bonds. Accordingly, the surface energies were calculated based on the literature⁷⁰ and are shown in Table 1 (see also the ESI and Table S1†). The surface energies were similar for unmodified and PEDOT:PSS-modified ITO (72 mJ m⁻² and 73 mJ m⁻²), whereas the surface energy of P3CPenT NW-modified ITO was lower at 55 mJ m⁻².

Deconvolution of the surface energy into dispersion surface energy, γ_s^d , and hydrogen bond surface energy, γ_s^h , components indicates that the γ_s^h is responsible for the reduced surface energy of P3CPenT modified interfaces as seen in Table 1. The surface

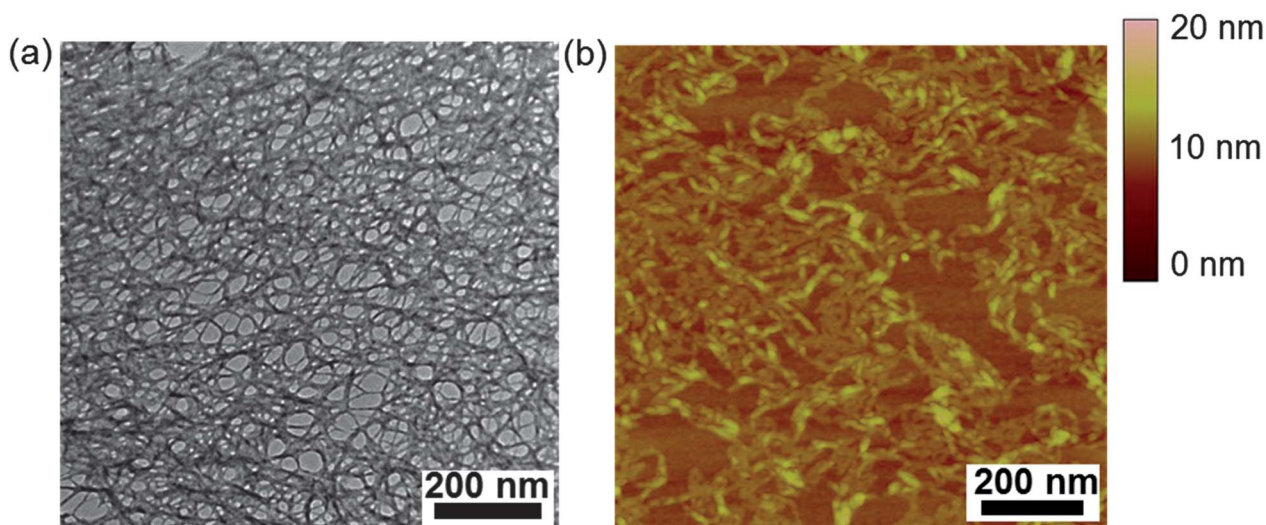


Fig. 3 (a) TEM image of P3CPenT NWs, and (b) AFM height image of P3CPenT NWs on silicon.

energy of substrates has considerable influence over concentration gradients in BHJ photoactive layers and hence influences the PSC device performance.^{30,71} Because P3HT has a lower surface energy than PCBM, when hydrophilic PEDOT:PSS is used as the HTL, P3HT tends to accumulate near the air/BHJ interface while PCBM accumulates closer to the hydrophilic PEDOT:PSS HTLs.³⁰ This surface-induced concentration of PCBM near the anode is detrimental to forward mode PSC operation as a more uniform distribution of P3HT and PCBM (or, possibly even more advantageous, a greater P3HT content near the anode) would be preferred to reduce recombination.^{30,71} As has been suggested previously,³⁰ gradient formation occurs during the solvent evaporation step following spin-coating, and decreasing the surface energy of the anode tends to reduce the magnitude of concentration gradients. For example, Baik *et al.* introduced a thin layer of P3HT with low surface energy between PEDOT:PSS and the P3HT:PCBM active layer, encouraging PCBM to accumulate at the top of the active layer.⁷²

The influence of the HTL surface energy over the morphology of P3HT:PCBM BHJ films was studied by cross sectional TEM imaging. Samples consisting of P3HT:PCBM spin-cast on various HTLs were prepared on silicon substrates, and cross-sectional TEM images were collected for each. These images are presented in Fig. 6 (and also Fig. S3–S5 in the ESI†), along with the associated TEM signal intensity profiles. Control samples consisting only of carbon prepared under the same conditions are uniformly bright, as shown in Fig. S6†, indicating that thickness variations in the TEM samples are not large and do not significantly contribute to variations in the intensity profile. Therefore, based on electron density, bright regions in Fig. 6 indicate increased P3HT content while darker regions correspond to areas of greater PCBM concentration.⁷³ Distinct PEDOT:PSS and P3CPenT layers are clearly observed in Fig. 6b and c. For the unmodified and PEDOT:PSS-modified substrates in Fig. 6a and b, dark regions are obvious near the Si substrates, and brighter regions are prevalent closer to the BHJ/air interface. This gradient indicates that PCBM accumulates near the HTL. Using P3CPenT in place of PEDOT:PSS (Fig. 6c), we observed

a uniform TEM image intensity, indicating a homogeneous distribution of P3HT and PCBM throughout the film. This more uniform distribution of P3HT and PCBM is expected to improve the device performance of solar cells.

3.4 Performance of photovoltaic devices

The properties P3CPenT as an HTL were investigated using P3HT:PCBM as a photoactive layer in an ITO/HTL/P3HT:PCBM/LiF/Al architecture under AM 1.5 G simulated solar illumination. The influence of P3CPenT thickness over device performance was investigated as shown in Fig. 7a, and the photovoltaic parameters are summarized in Table 2. (Current density–voltage curves for devices fabricated with each of the P3CPenT thicknesses are also included in the ESI in Fig. S7 and S8†.) The spin-cast P3CPenT thickness ranged from 5 nm to 120 nm as determined by AFM (shown in Fig. S9 in the ESI†). It should be noted that these P3CPenT films were cast from higher concentration DMSO solution than those of Fig. 3, and thus considerably thicker, more interconnected films were formed. Devices including P3CPenT as an HTL performed considerably better than devices without a distinct interfacial layer: open circuit voltage (V_{OC}), fill factor (FF), and PCE increased. When the thickness of P3CPenT increased from 5 nm to 8 nm, short-circuit current density (J_{SC}) and V_{OC} remained roughly constant around $\sim 9 \text{ mA cm}^{-2}$ and 0.55 V, respectively, while the FF increased slightly from 0.61 to 0.67. The increased FF may originate from a reduced leakage current (*i.e.*, increased shunt resistance, R_{SH}), increasing surface area for charge collection through the interfacial layer on ITO, or reduced concentration of PCBM near the anode.³¹ As the thickness of P3CPenT further increased from 8 nm to 120 nm, V_{OC} , series resistance (R_S), R_{SH} and FF remained relatively constant. The stable R_S potentially indicates that the P3CPenT conductivity is relatively large, and that device resistance may be dominated by layers other than the HTL. The J_{SC} , however, gradually decreased from 9.3 mA cm^{-2} to 7.5 mA cm^{-2} as the P3CPenT thickness increased from 8 to 120 nm. This trend of decreasing J_{SC} with increasing P3CPenT

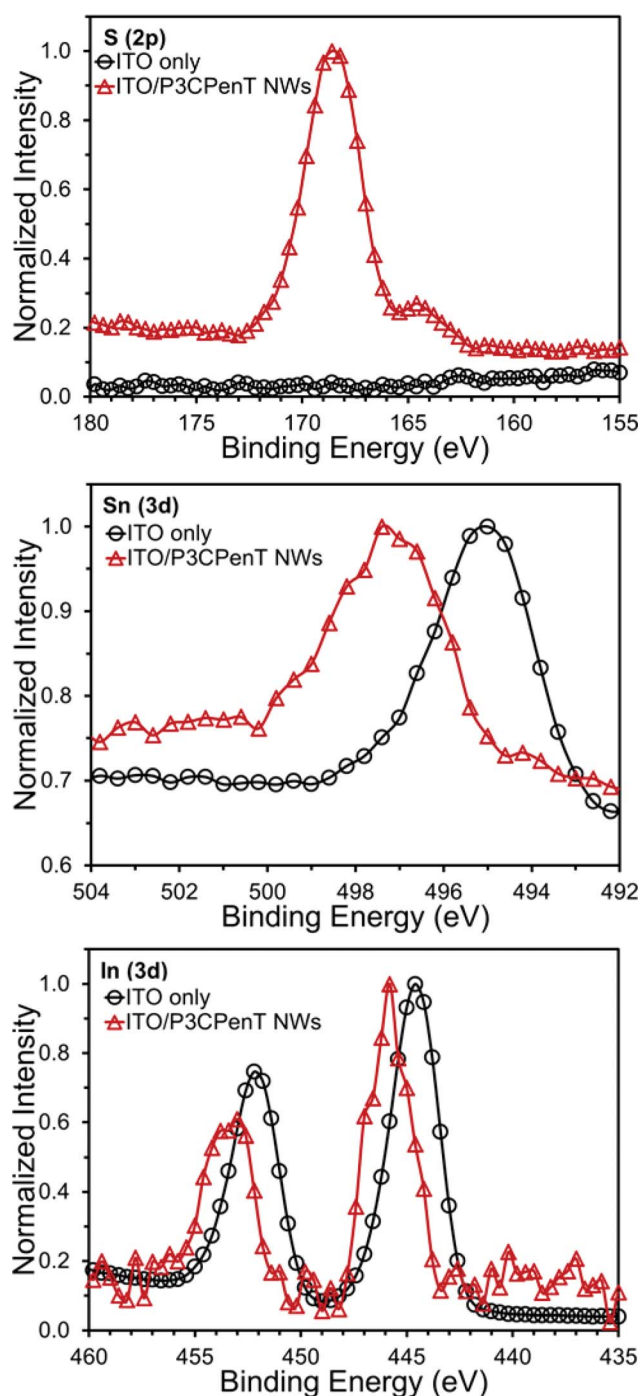


Fig. 4 XPS spectra of unmodified ITO, ITO modified by P3CpenT with absorption method and ITO modified by P3CpenT with spin coating method: (a) S(2p), (b) Sn(3d), and (c) In(3d).

thickness is more pronounced than the corresponding trend observed with PEDOT:PSS as an HTL. The thickness of PEDOT:PSS has less influence over P3HT:PCBM PSC performance, although the PCE decreases slightly (4.6% reduction from 30 nm to 160 nm) (see Fig. S10†).⁷⁴ The decreasing J_{SC} likely originates from light absorption by P3CpenT in the range 400–600 nm, which overlaps with the absorption band of P3HT as shown in Fig. S11 in the ESI†. Transmission spectra of ITO

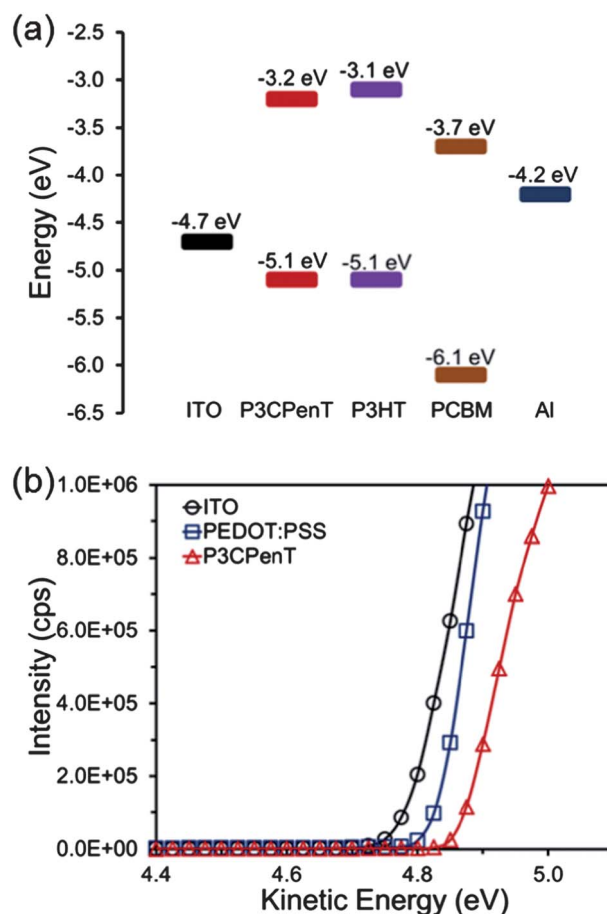


Fig. 5 (a) Energy levels of the electronic materials used in this study. The energy levels of P3CpenT, P3HT and PCBM were measured by electrochemical cyclic voltammetry. (b) UPS spectra used to calculate the work functions of bare ITO, ITO modified by P3CpenT (12 nm), and PEDOT:PSS (30 nm) from UPS measurement.

and ITO modified with different thicknesses of P3CpenT were measured and are shown in Fig. 7b. When the P3CpenT thickness increases from 0 nm (*i.e.*, only ITO) to 120 nm, the minimum transmission located at about 550 nm decreases from 85% (0 nm P3CpenT thickness) to 80% (8 nm) to 46% (120 nm), which reduces absorption of photons within the P3HT:PCBM active layer and consequently reduces the output current density. To determine the effect of P3CpenT crystallinity and the nanowire architecture, control experiments were also performed comparing more crystalline DMSO-cast HTLs to less crystalline pyridine-cast films (*vide supra*) in P3HT:PCBM PSC devices. In these experiments, DMSO-cast HTLs performed considerably better with superior J_{SC} , FF, R_s , and R_{SH} (see Table S2†). The PCE of DMSO-cast devices were 23% greater than pyridine-cast devices, indicating the importance of crystallinity in the HTL to facilitate efficient charge extraction.

P3HT:PCBM BHJ solar cells with optimized PEDOT:PSS and P3CpenT HTLs were investigated in detail and compared to devices fabricated without HTLs. The resulting current density–voltage ($J-V$) curves are shown in Fig. 8, and the extracted PV parameters are summarized in Table 3. The control device operating without a distinct HTL performed poorly, but when

Table 1 Contact angles and surface energies of ITO surfaces modified with PEDOT:PSS or P3CPenT

	Water contact angle (°)	<i>n</i> -Hexadecane contact angle (°)	Dispersion surface energy, γ_s^d (mJ m ⁻²)	Hydrogen bonding surface energy, γ_s^h (mJ m ⁻²)	Surface energy, γ_s (mJ m ⁻²)
Unmodified ITO	9	9	27	45	72
ITO modified by PEDOT:PSS	4	10	27	46	73
ITO modified by P3CPenT	47	3	28	27	55

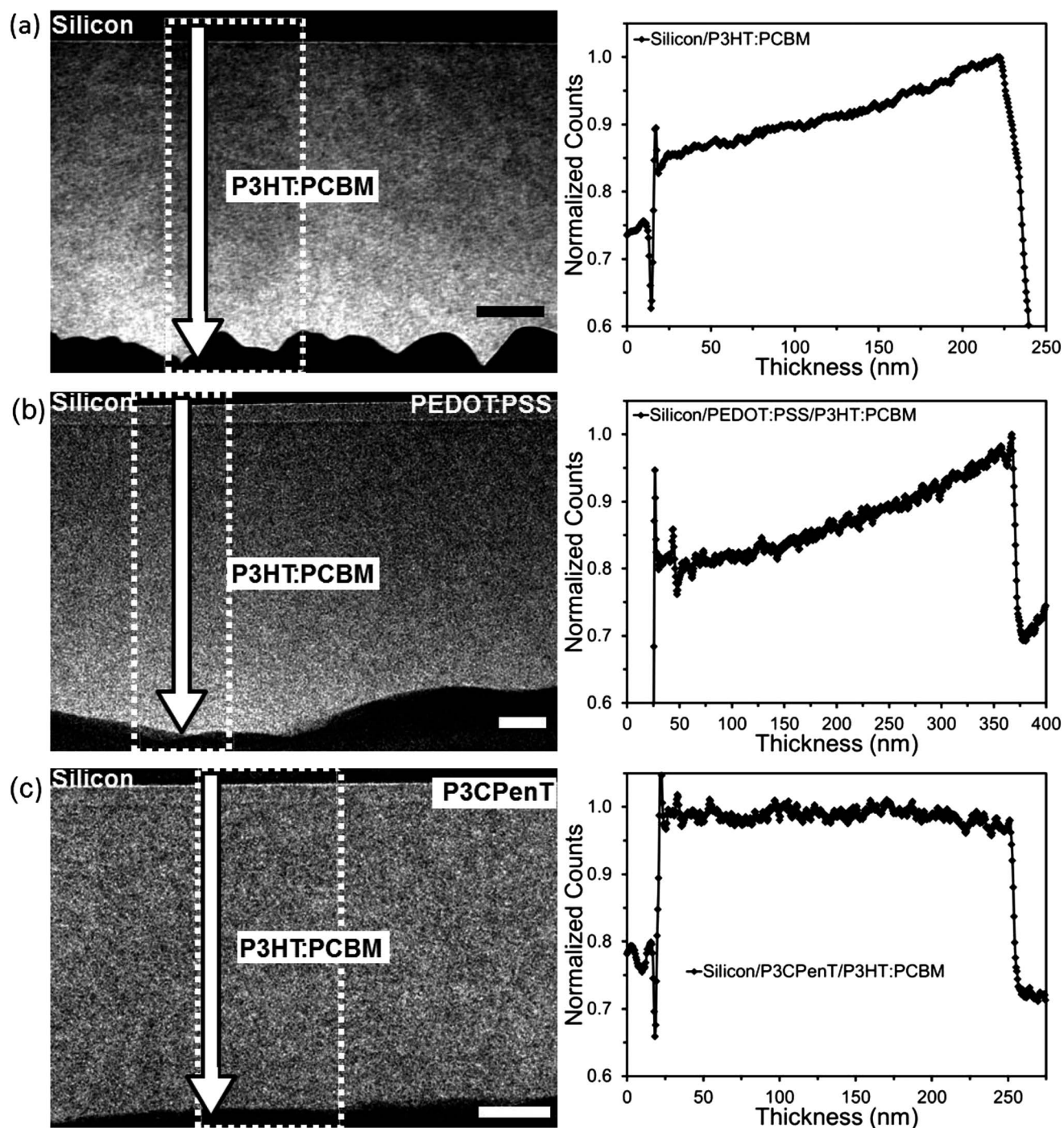


Fig. 6 Cross sectional TEM images and intensity profiles along the direction perpendicular to the interfaces of P3HT:PCBM film on (a) unmodified Si substrate; (b) modified Si substrate by PEDOT:PSS and (c) modified Si substrate by P3CPenT. The profiles are the normalized average counts in the dashed boxes in the TEM images. The scale bars in the TEM images are 50 nm.

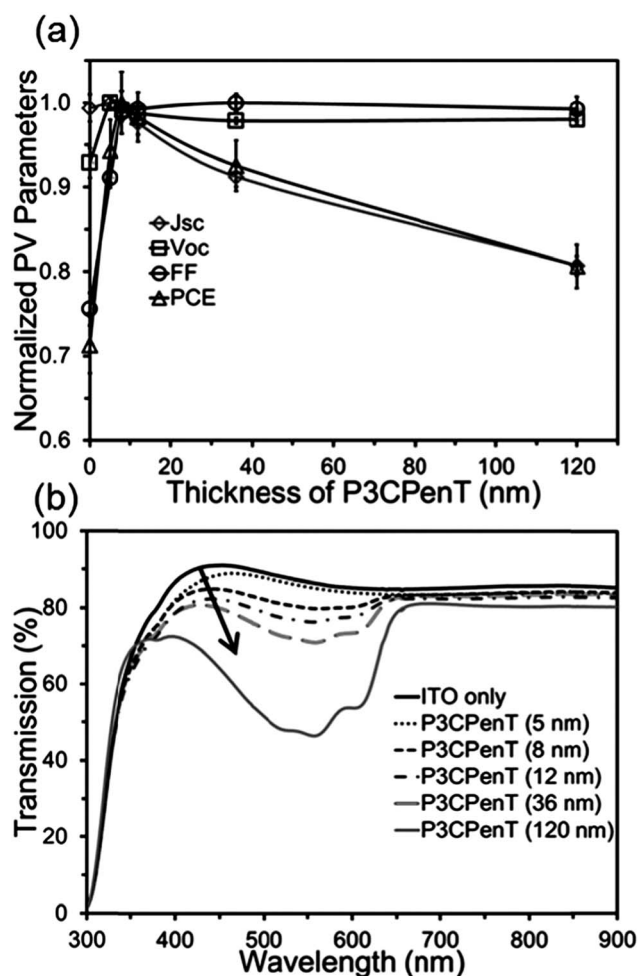


Fig. 7 Influence of P3CPenT HTL thickness over PSC performance. (a) Plot of PV characteristics for devices fabricated with different thicknesses of P3CPenT. Each point represents the average of 4 PV devices. (b) Transmission spectra of ITO and ITO modified with different thicknesses of P3CPenT.

P3CPenT (8 nm) or PEDOT:PSS (30 nm) were introduced, the J_{SC} remained constant, while both V_{OC} and FF increased. The increase in V_{OC} and FF may originate from the increased shunt resistance (R_{SH}) as shown in Table 3, compared with low R_{SH} induced by leakage current in samples without HTLs.⁷⁵ Comparing devices with PEDOT:PSS and P3CPenT HTLs, we found that the J_{SC} and V_{OC} were approximately similar, while

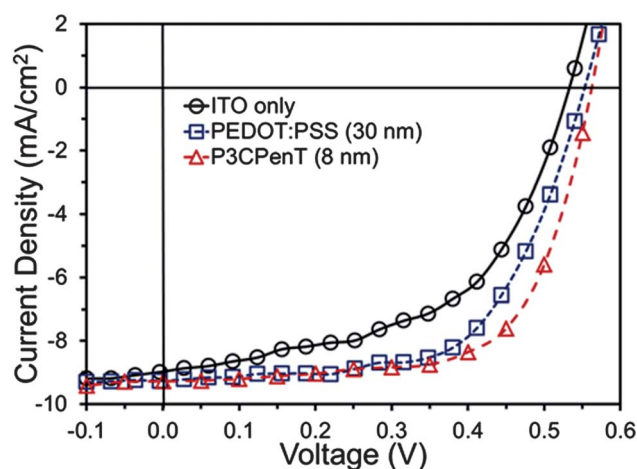


Fig. 8 Current density–voltage characteristics of photovoltaic devices with ITO only, PEDOT:PSS (30 nm), and P3CPenT (12 nm) as an HTL. Dark curves are provided in the ESI in Fig. S13†.

the FF improved from 0.61 to 0.67 and the R_S decreased from 8.17 Ω cm² to 6.45 Ω cm² when PEDOT:PSS was replaced with P3CPenT. We propose that the increased FF may partially originate from the following three factors: (1) the increased work function of P3CPenT NW-modified films, reducing the energy barrier for hole extraction;⁷⁶ (2) elimination of the P3HT:PCBM concentration gradient provides better routes for hole transport, reducing charge recombination at the P3HT/HTL interface for forward solar cells; and (3) improved hole transport through semi-crystalline P3CPenT nanowires.⁵⁴ Finally, devices incorporating P3CPenT as an interfacial layer gave an average PCE of 3.4%, outperforming PEDOT:PSS PSCs and indicating that P3CPenT NWs could replace PEDOT:PSS in P3HT:PCBM solar cells.

Device stability was also investigated, and the results are shown in the ESI in Fig. S12†. For both PEDOT:PSS and P3CPenT-based devices, the V_{OC} was roughly constant, while the J_{SC} and FF decreased over time. For PEDOT:PSS, the PCE maintained 57% of its original value after 78 days, and for P3CPenT, the PCE maintained 64% of its original value after the same time period. Although the difference is neither large nor clear, the greater value for P3CPenT devices may be attributable to reduced ITO etching because Na⁺PSS⁻ has been shown to slowly etch ITO⁷⁷ and/or corrode the Al electrode after diffusion through the active layer.^{24,25} The poor lifetime for these cells may,

Table 2 Summary of PV characteristics of the BHJ OPVs including averages of four devices and standard deviations (in parentheses) of the short circuit current density (J_{SC}), open circuit voltage (V_{OC}), fill factor (FF) and power conversion efficiency (PCE) with different thickness of P3CPenT as HTL

Thickness of P3CPenT (nm)	J_{SC} (mA cm ⁻²)	V_{OC} (V)	FF	PCE (%)	R_S (Ω cm ²)	R_{SH} (k Ω cm ²)
0	9.2 (0.2)	0.52 (0.01)	0.51 (0.01)	2.4 (0.1)	6.0 (0.1)	0.34 (0.09)
5	9.3 (0.1)	0.559 (0.004)	0.610 (0.007)	3.2 (0.1)	6.8 (0.3)	1.7 (0.1)
8	9.3 (0.2)	0.555 (0.002)	0.666 (0.006)	3.4 (0.1)	6.5 (0.2)	1.81 (0.04)
12	9.1 (0.1)	0.553 (0.002)	0.665 (0.006)	3.4 (0.1)	6.5 (0.1)	1.88 (0.05)
36	8.5 (0.1)	0.548 (0.002)	0.670 (0.007)	3.2 (0.1)	6.2 (0.2)	1.86 (0.07)
120	7.5 (0.1)	0.549 (0.004)	0.67 (0.01)	2.8 (0.1)	6.1 (0.1)	1.92 (0.06)

Table 3 Average photovoltaic parameters of four devices fabricated with only ITO, PEDOT:PSS (30 nm), and P3CPenT (8 nm) as HTL. Standard deviations are included in parentheses

HTL	J_{SC} (mA cm ⁻²)	V_{OC} (V)	FF	PCE (%)	R_S (Ω cm ²)	R_{SH} (k Ω cm ²)	Best PCE (%)
ITO only	9.2 (0.2)	0.52 (0.01)	0.51 (0.01)	2.4 (0.1)	6.0 (0.1)	0.34 (0.09)	2.5
PEDOT:PSS	9.2 (0.1)	0.55 (0.003)	0.61 (0.01)	3.1 (0.1)	8.2 (0.1)	1.78 (0.03)	3.4
P3CPenT	9.3 (0.2)	0.56 (0.002)	0.67 (0.01)	3.4 (0.1)	6.5 (0.2)	1.81 (0.04)	3.7

however, also be dominated by degradation of the low work function cathode and reactions with the active layer materials in the forward-mode solar cells.^{78,79}

4. Conclusions

A carboxylated poly(3-hexylthiophene) derivative, P3CPenT, was used as a hole transport layer between a transparent ITO electrode and P3HT:PCBM photoactive layer. P3CPenT has several desirable properties as an HTL, including solubility only in certain polar solvents (that do not match the solvents for solubilizing P3HT:PCBM) and energy levels similar to P3HT. Moreover, P3CPenT films formed a nanowire network when cast from DMSO solution, and ITO surfaces modified with P3CPenT were found to be lower in surface energy than those modified with PEDOT:PSS. This property reduces the tendency of P3HT:PCBM photoactive layers cast above P3CPenT to form concentration gradients with an increased PCBM concentration near the hole-collecting anode. Consequently, photovoltaic devices with P3CPenT HTLs showed improved FF (0.67) and PCE, as compared to devices with PEDOT:PSS HTLs. These properties collectively point toward a generalized strategy to exploit conjugated donors in combination with their carboxylated derivatives: the pairs may have orthogonal solubilities yet matching electronics, and lead to improved BHJ morphologies without additional heating and processing steps.

Acknowledgements

The authors acknowledge support from the Natural Sciences and Engineering Research Council Canada, NRC-NINT, Alberta Innovates Technology Futures and the University of Alberta School of Energy and the Environment. We gratefully acknowledge the Alberta Centre for Surface Engineering and Science for UPS measurements, Dr Jonathan Veinot for access to the top contact evaporator, and Dr Erik Luber for helpful discussions on surface energy.

Notes and references

- N. S. Sariciftci, L. Smilowitz, A. J. Heeger and F. Wudl, *Science*, 1992, **258**, 1474.
- C. J. Brabec, S. Gowrisanker, J. J. M. Halls, D. Laird, S. Jia and S. P. Williams, *Adv. Mater.*, 2010, **22**, 3839.
- C. Deibel and V. Dyakonov, *Rep. Prog. Phys.*, 2010, **73**, 096401.
- G. Yu, J. Gao, J. C. Hummelen, F. Wudl and A. J. Heeger, *Science*, 1995, **270**, 1789.
- S. K. Hau, H. L. Yip and A. K. Y. Jen, *Polym. Rev.*, 2010, **50**, 474.
- Y. Liang and L. Yu, *Acc. Chem. Res.*, 2010, **43**, 1227.
- H. Y. Chen, J. Hou, S. Zhang, Y. Liang, G. Yang, Y. Yang, L. Yu, Y. Wu and G. Li, *Nat. Photonics*, 2009, **3**, 649.
- Y. Liang, Z. Xu, J. Xia, S. T. Tsai, Y. Wu, G. Li, C. Ray and L. Yu, *Adv. Mater.*, 2010, **22**, E135.

- C. M. Amb, S. Chen, K. R. Graham, J. Subbiah, C. E. Small, F. So and J. R. Reynolds, *J. Am. Chem. Soc.*, 2011, **133**, 10062.
- H. Zhou, L. Yang, A. C. Stuart, S. C. Price, S. Liu and W. You, *Angew. Chem., Int. Ed.*, 2011, **50**, 2995.
- T. Y. Chu, J. Lu, S. Beaupre, Y. Zhang, J. R. Pouliot, S. Wakim, J. Zhou, M. Leclerc, Z. Li, J. Ding and Y. Tao, *J. Am. Chem. Soc.*, 2011, **133**, 4250.
- Z. He, C. Zhong, X. Huang, W. Y. Wong, H. Wu, L. Chen, S. Su and Y. Cao, *Adv. Mater.*, 2011, **23**, 4636.
- H. Ma, H. L. Yip, F. Huang and A. K. Y. Jen, *Adv. Funct. Mater.*, 2010, **20**, 1371.
- L. M. Chen, Z. Xu, Z. Hong and Y. Yang, *J. Mater. Chem.*, 2010, **20**, 2575.
- R. Po, C. Carbonera, A. Bernardi and N. Camaioni, *Energy Environ. Sci.*, 2011, **4**, 285.
- J. H. Park, T. W. Lee, B. D. Chin, D. H. Wang and O. O. Park, *Macromol. Rapid Commun.*, 2010, **31**, 2095.
- N. S. Kang, B. K. Ju, C. Lee, J. P. Ahn, B. D. Chin and J. W. Yu, *Org. Electron.*, 2009, **10**, 1091.
- C. P. Chen, T. C. Tien, B. T. Ko, Y. D. Chen and C. Ting, *ACS Appl. Mater. Interfaces*, 2009, **1**, 741.
- J. Ouyang, C. W. Chi, F. C. Chen, Q. Xu and Y. Yang, *Adv. Funct. Mater.*, 2005, **15**, 203.
- X. Crispin, F. L. E. Jakobsson, A. Crispin, P. C. M. Grim, P. Andersson, A. Volodin, C. van Haesendonck, M. Van der Auweraer, W. R. Salaneck and M. Berggren, *Chem. Mater.*, 2006, **18**, 4354.
- Y. H. Kim, S. H. Lee, J. Noh and S. H. Han, *Thin Solid Films*, 2006, **510**, 305.
- E. Voroshazi, B. Verreet, A. Buri, R. Muller, D. D. Nuzzo and P. Heremans, *Org. Electron.*, 2011, **12**, 736.
- K. Kawano, R. Pacios, D. Poplavskyy, J. Nelson, D. D. C. Bradley and J. R. Durrant, *Sol. Energy Mater. Sol. Cells*, 2006, **90**, 3520.
- K. Norrman, N. B. Larsen and F. C. Krebs, *Sol. Energy Mater. Sol. Cells*, 2006, **90**, 2793.
- K. Norrman, S. A. Gevorgyan and F. C. Krebs, *ACS Appl. Mater. Interfaces*, 2009, **1**, 102.
- A. M. Nardes, M. Kemerink, M. M. de Kok, E. Vinken, K. Maturova and R. A. J. Janssen, *Org. Electron.*, 2008, **9**, 727.
- J. Subbiah, D. Y. Kim, M. Hartel and F. So, *Appl. Phys. Lett.*, 2010, **96**, 063303.
- F. C. Chen, Y. K. Lin and C. J. Ko, *Appl. Phys. Lett.*, 2008, **92**, 023307.
- C. Waldauf, M. Morana, P. Denk, P. Schilinsky, K. Coakley, S. A. Choulis and C. J. Brabec, *Appl. Phys. Lett.*, 2006, **89**, 233517.
- Z. Xu, L. M. Chen, G. Yang, C. H. Huang, J. Hou, Y. Wu, G. Li, C. S. Hsu and Y. Yang, *Adv. Funct. Mater.*, 2009, **19**, 1227.
- M. D. Irwin, D. B. Buchholz, A. W. Hains, R. P. H. Chang and T. J. Marks, *Proc. Natl. Acad. Sci. U. S. A.*, 2008, **105**, 2783.
- N. Sun, G. Fang, P. Qin, Q. Zheng, M. Wang, X. Fan, F. Cheng, J. Wan, X. Zhao, J. Liu, D. L. Carroll and J. Ye, *J. Phys. D: Appl. Phys.*, 2010, **43**, 445101.
- S. Y. Park, H. R. Kim, Y. J. Kang, D. H. Kim and J. W. Kang, *Sol. Energy Mater. Sol. Cells*, 2010, **94**, 2332.
- K. X. Steirer, J. P. Chesin, N. E. Widjonarko, J. J. Berry, A. Miedaner, D. S. Ginley and D. C. Olson, *Org. Electron.*, 2010, **11**, 1414.
- S. Han, W. S. Shin, M. Seo, D. Gupta, S. J. Moon and S. Yoo, *Org. Electron.*, 2009, **10**, 791.
- F. Liu, S. Shao, X. Guo, Y. Zhao and Z. Xie, *Sol. Energy Mater. Sol. Cells*, 2010, **94**, 842.
- G. H. Jung, K. G. Lim, T. W. Lee and J. L. Lee, *Sol. Energy Mater. Sol. Cells*, 2011, **95**, 1146.

- 38 V. Shrotriya, G. Li, Y. Yao, C. W. Chu and Y. Yang, *Appl. Phys. Lett.*, 2006, **88**, 073508.
- 39 S. Shao, F. Liu, Z. Xie and L. Wang, *J. Phys. Chem. C*, 2010, **114**, 9161.
- 40 S. W. Tong, C. F. Zhang, C. Y. Jiang, G. Liu, Q. D. Ling, E. T. Kang, D. S. H. Chan and C. Zhu, *Chem. Phys. Lett.*, 2008, **453**, 73.
- 41 A. W. Hains, C. Ramanan, M. D. Irwin, J. Liu, M. R. Wasielewski and T. J. Marks, *ACS Appl. Mater. Interfaces*, 2010, **2**, 175.
- 42 S. Berny, L. Tortech, M. Veber and D. Fichou, *ACS Appl. Mater. Interfaces*, 2010, **2**, 3059.
- 43 S. S. Li, K. H. Tu, C. C. Lin, C. W. Chen and M. Chhowalla, *ACS Nano*, 2010, **4**, 3169.
- 44 H. Y. Wei, J. H. Huang, K. C. Ho and C. W. Chu, *ACS Appl. Mater. Interfaces*, 2010, **2**, 1281.
- 45 C. W. Liang, W. F. Su and L. Wang, *Appl. Phys. Lett.*, 2009, **95**, 133303.
- 46 G. K. R. Senadeera, K. Nakamura, T. Kitamura, Y. Wada and S. Yanagida, *Appl. Phys. Lett.*, 2003, **83**, 5470.
- 47 J. K. Lee, W. S. Kim, H. J. Lee, W. S. Shin, S. H. Jin, W. K. Lee and M. R. Kim, *Polym. Adv. Technol.*, 2006, **17**, 709.
- 48 K. Shankar, G. K. Mor, H. E. Prakasam, O. K. Varghese and C. A. Grimes, *Langmuir*, 2007, **23**, 12445.
- 49 J. Liu, E. N. Kadnikova, Y. Liu, M. D. McGehee and J. M. J. Frechet, *J. Am. Chem. Soc.*, 2004, **126**, 9486.
- 50 F. C. Krebs, *Sol. Energy Mater. Sol. Cells*, 2008, **92**, 715.
- 51 C. J. Bhongale and M. Thelakkat, *Sol. Energy Mater. Sol. Cells*, 2010, **94**, 817.
- 52 M. Thomas, B. J. Worfolk, D. A. Rider, M. T. Taschuk, J. M. Buriak and M. J. Brett, *ACS Appl. Mater. Interfaces*, 2011, **3**, 1887.
- 53 B. J. Worfolk, D. A. Rider, A. L. Elias, M. Thomas, K. D. Harris and J. M. Buriak, *Adv. Funct. Mater.*, 2011, **21**, 1816.
- 54 H. Xin, F. S. Kim and S. A. Jenekhe, *J. Am. Chem. Soc.*, 2008, **130**, 5424.
- 55 H. Xin, O. G. Reid, G. Ren, S. Kim, D. S. Ginger and S. A. Jenekhe, *ACS Nano*, 2010, **4**, 1861.
- 56 G. Ren, P. T. Wu and S. A. Jenekhe, *ACS Nano*, 2011, **5**, 376.
- 57 P. T. Wu, G. Q. Ren, C. Li, R. Mezzenga and S. A. Jenekhe, *Macromolecules*, 2009, **42**, 2317.
- 58 P. T. Wu, H. Xin, F. S. Kim, G. Ren and S. A. Jenekhe, *Macromolecules*, 2009, **42**, 8817.
- 59 H. Xin, G. Ren, F. S. Kim and S. A. Jenekhe, *Chem. Mater.*, 2008, **20**, 6199.
- 60 S. Berson, R. D. Bettignies, S. Bailly and S. Guillerez, *Adv. Funct. Mater.*, 2007, **17**, 1377.
- 61 G. Lu, H. Tang, Y. Qu, L. Li and X. Yang, *Macromolecules*, 2007, **40**, 6579.
- 62 J. A. Merlo and C. D. Frisbie, *J. Phys. Chem. B*, 2004, **108**, 19169.
- 63 K. J. Ihn, J. Moulton and P. Smith, *J. Polym. Sci., Part B: Polym. Phys.*, 1993, **31**, 735.
- 64 R. Osterbacka, C. P. An, X. M. Jiang and Z. V. Vardeny, *Science*, 2000, **287**, 839.
- 65 T. Erb, U. Zhokhavets, G. Gobsch, S. Raleva, B. Stuhn, P. Schilinsky, C. Waldauf and C. J. Brabec, *Adv. Funct. Mater.*, 2005, **15**, 1193.
- 66 R. D. McCullough, P. C. Ewbank and R. S. Loewe, *J. Am. Chem. Soc.*, 1997, **119**, 633.
- 67 P. Markiewicz and M. C. Goh, *Langmuir*, 1994, **10**, 5.
- 68 S. A. Paniagua, P. J. Hotchkiss, S. C. Jones, S. R. Marder, A. Mudalige, F. S. Marrikar, J. E. Pemberton and N. R. Armstrong, *J. Phys. Chem. C*, 2008, **112**, 7809.
- 69 G. Li, C. W. Chu, V. Shrotriya, J. Huang and Y. Yang, *Appl. Phys. Lett.*, 2006, **88**, 253503.
- 70 D. K. Owens and R. C. Wendt, *J. Appl. Polym. Sci.*, 1969, **13**, 1741.
- 71 A. S. Anselmo, L. Lindgren, J. Rysz, A. Bernasik, A. Budkowski, M. R. Andersson, K. Svensson, J. van Stam and E. Moons, *Chem. Mater.*, 2011, **23**, 2295.
- 72 J. Y. Oh, W. S. Jang, T. I. Lee, J. M. Myoung and H. K. Baik, *Appl. Phys. Lett.*, 2011, **98**, 023303.
- 73 W. Li, Y. Zhou, B. V. Andersson, L. M. Andersson, Y. Thomann, C. Veit, K. Tvingstedt, R. P. Qin, Z. Bo, O. Inganäs, U. Wurfel and F. Zhang, *Org. Electron.*, 2011, **12**, 1544.
- 74 Y. Kim, A. M. Ballantyne, J. Nelson and D. D. C. Bradley, *Org. Electron.*, 2009, **10**, 205.
- 75 H. Xu, L. Yang, H. Tian, S. Yin and F. Zhang, *Optoelectron Lett.*, 2010, **6**, 176.
- 76 M. S. Kim, B. G. Kim and J. Kim, *ACS Appl. Mater. Interfaces*, 2009, **1**, 1264.
- 77 C. W. T. Bulle-Lieuwma, W. J. H. van Gennip, J. K. J. van Duren, P. Jonkheijm, R. A. J. Janssen and J. W. Niemantsverdriet, *Appl. Surf. Sci.*, 2003, **203**, 547.
- 78 M. Jorgensen, K. Norrman and F. C. Krebs, *Sol. Energy Mater. Sol. Cells*, 2008, **92**, 686.
- 79 J. Nishinaga, T. Aihara, H. Yamagata and Y. Horikoshi, *J. Cryst. Growth*, 2005, **278**, 633.